Experimental modal analysis of a full-scale rotating fan

Corentin Jorajuria, Claude Gibert, Fabrice Thouverez, Cécile Esteves

Experimental modal analysis of a full-scale rotating fan

Corentin Jorajuria[1,2*], Cécile Esteves[2], Claude Gibert[1] and Fabrice Thouverez[1]

[1] Ecole Centrale de Lyon, CNRS, ENTPE, Laboratoire de Tribologie et Dynamique des Systèmes, UMR5513
[2] Safran Aircraft Engines, Safran Group

Abstract

Experimental modal analysis of a full-scale aeronautic fan is performed at design rotating speed and under vacuum conditions. The composite woven fan is excited through embedded piezoelectric actuators and the dynamic response of the system is measured with strain gauges. Presented experiments achieve high quality data measurements of forced responses thanks to a strict control of experimental conditions, an extended instrumentation of the fan and a careful testing method. The study focuses on the two first bending mode families with nodal diameters. The modal testing of the system is performed using frequency stepped sine excitations over a close range around investigated resonances and using travelling wave excitations allowing to investigate specific nodal diameter modes in each family. The forced response measurements are used to estimate the frequency response functions of the rotating fan under different experimental parameters. In particular, the first mode family exhibits a higher modal density which is challenging for modal parameters estimations. Used frequency domain modal identification techniques are presented and adapted to the fitting of frequency response functions. At the end, these techniques are applied to investigate sensitivity of extracted natural frequencies and modal damping ratios with respect to different parameters such as rotational speed, excitation level and nodal diameter content of the excitation pattern.

Keywords: modal testing, vacuum conditions, piezoelectric actuators, rotating fan, frequency domain identification.

Introduction

Innovative turbojet engine designs have led to increasing demand for precise dynamics prediction and analysis. Among these issues energy dissipation mechanisms have long been related to popular but challenging topics. Presented study addresses the issue of experimental dynamics analysis of a composite woven fan at design rotation speed and in vacuum conditions, thus focusing on mechanical phenomena. Previous studies at Ohio State University analyzed bladed disk dynamics experimentally using air jet devices to impose synchronous and asynchronous excitations [1] [2]. Different experimental framework from air jet excitations consists in bounding piezoelectric actuators on the system. Such actuator systems have been used successfully to reduce vibrations of a mistuned blisk [3]. At Ecole Centrale de Lyon experimental investigations over passive reduction vibration with friction interfaces have also been conducted using piezoelectric actuators [4]. To perform accurate analysis of these experiments appropriate estimation methods are necessary. For instance, model response used for parameters estimation can take into account nonlinear dynamics when such effects contribute significantly [5]. This article presents experiments and appropriate estimation method to investigate first and second blade bending modes of a rotating fan using asynchronous excitations through piezoelectric actuators extending first results of PHARE#1 test rig [6]. First section presents the experimental procedures used to investigate the fan specimen. Techniques used to estimate the modal parameters from the frequency response functions data are presented in second section. Last section presents sensitivity of extracted natural frequencies and damping ratios with respect to rotational speed and amplitude of excitation.

*Corresponding author: corentin.jorajuria@ec-lyon.fr
Received: April 11, 2022, **Published:** October 28, 2022

1 Experimental procedures

This section presents experimental procedures adopted to measure frequency responses of a full-scale rotating fan in vacuum conditions. The particular test rig used to measure the system dynamics is presented in a first subsection. Second subsection presents the adopted testing protocol.

1.1 Experimental facility

The experiments are performed using PHARE#1 experimental facility which focus on measuring full scale rotating machine dynamics during rotation and in vacuum conditions. A cross-section view of the facility is presented in figure 1.

The fan specimen is mounted on the shaft of a supporting test vehicle. This test vehicle is placed in a cylindrical vacuum chamber with inside dimension 3 m of diameter and 4 m along the axis. The vacuum chamber is strongly fixed to a seismic concrete mass mounted on suspension springs and dampers in order to dynamically isolate the test rig from the environment and prevent from critical vibration levels in case of heavy accidental load. The access to the vacuum chamber is made through a front door which goes down in the floor below when opened and which is

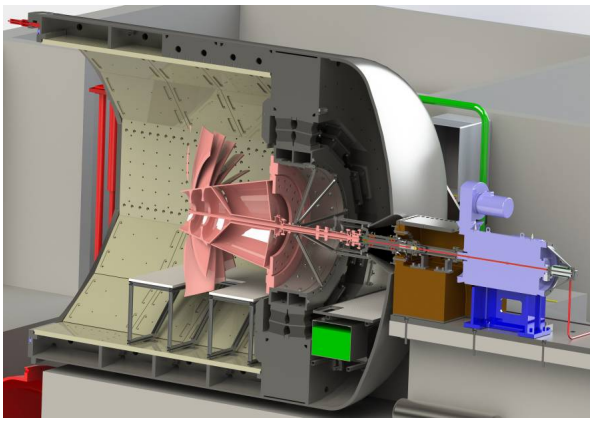

Figure 1: *Cross-section view of the experimental facility.*

sealed to the chamber's wall with pneumatic joints. Special dynamic sealing of the driving shaft through the chamber's wall is operated with a circumferential carbon ring seal. A double stage rotating vane vacuum pump associated with a Roots pump keeps the pressure inside the vacuum chamber at 0.1 *mbar*. A 700 *kW* electric driving motor allows fast ramp up and down in vacuum as well as driving speed up to 8000 *rpm* for low pressure stage applications. A hydraulic group ensures the lubrication of the bearings of the test vehicle in vacuum environment. Blades of the fan specimen are numbered according to direction of rotation with $p = 1..n_s$ where n_s denotes the number of sectors each containing one blade. Each of the blades is instrumented with a set of interconnected piezoelectric patches composed of Lead Zirconate Titanate (PZT-5H). The piezoelectric characteristics and distribution on pressure side and suction side have been designed to reach significative vibration amplitude for first and second blade bending modes. Figure 2 illustrates one instrumented blade. An excitation generation system including a software, an electronic card signal generator and a multichannel power amplifier produces the signal for each actuator according to a desired pattern and level of excitation. Possible patterns include travelling waves generated by controlling phase difference between piezoelectric set associated to each blade. The amplified signals are passed to rotating frame thanks to a slip ring assembly with 36 circuits, then through the vacuum chamber wall using wires and connector stages placed into the hollow driving shaft. Each blade is instrumented with two strain gauges positioned to optimize strain measurements in the direction of the gauge for first and second blade bending modes taking into account assembling constraints. The electromagnetic compatibility between measurements circuit and actuators power feed circuit has been taken into account at design and checked in order to prevent measurements to be altered by electromagnetic influences. Strain gauges measurement signals are passed through the shaft of the test rig to a telemetry unit embedded in the driving shaft. The telemetry unit sends the rotating fan measurement signals to the data acquisition system. Strain gauges measurement

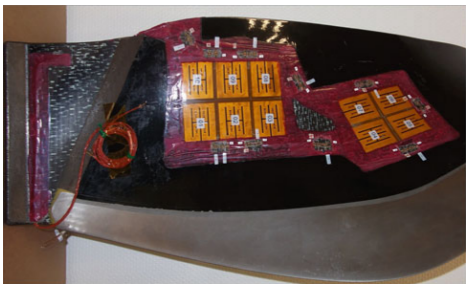

Figure 2: *One instrumented blade [7].*

signals are sampled at $f_s = 2 \cdot 10^3\ Hz$. Temperature monitoring is provided by embedded thermocouples and thermal imaging camera. In addition to temperature measurements the instrumentation of the test rig provides pressure and overall dynamics monitoring making the acquisition system manage more than 150 signals. A specifically designed software receiving signals from the acquisition system takes over commands of the rotation of the test vehicle and the monitoring of the overall dynamics of the test rig. An independent software controls the piezoelectric actuators for vibration tests including excitation signal generation, sending commands for the excitation system and receiving measurements from the acquisition system.

1.2 Testing protocol

Phare#1 test facility provides means to perform careful testing protocol. The adopted testing protocol takes advantage of the massive instrumentation of the test rig to produce high quality frequency response measurements.

Presented results discuss the influence of rotation speed over the fan dynamics using three rotation speeds 30, 50 and 70% of nominal rotation speed denoted Ω_n. Vibration measurements have been performed at stabilized rotation speed. Dynamics of the fan specimen are investigated using stepped sine excitations with travelling wave pattern with nodal diameters. Stepped sine signals benefit from focusing high energy level on investigated frequencies and aiming at measuring steady state of the system. Stepped sine modal testing is for instance particularly adapted for modal testing of nonlinear systems. This technique is accurate but time consuming and estimation techniques have been developed both to reduce time and control accuracy of frequency response measurements [8] [9]. The test rig makes possible to impose a travelling wave excitation to investigate preferentially modes with specific nodal diameters mode shape. Presented dynamics analysis of the fan specimen focuses on the first and second bending blade mode of the rotating fan, in particular modes with nodal diameters 2, 3 and 4. Excitation signal sent to piezoelectric actuators is formally

presented in equation (1).

$$u_p(t) = a\sin\left(\omega(t)t - \frac{2\pi}{n_s}dp\right) \qquad (1)$$
$$\omega(t) = 2\pi f(t) \qquad \text{with } f(t) \text{ stepped function}$$
$$\text{from } f_{ini} \text{ to } f_{end} \text{ by } \delta f \text{ during } n_{exci} \text{ oscillations}$$

Where $p = 0..n_s - 1$ indexes the blade in the direction of rotation, a denotes the amplitude of the excitation signal and d gives the nodal diameters of the excitation pattern. Parameters f_{ini} and f_{end} denote the initial and final frequencies of the stepped signal, δf is the constant frequency step taken by the stepped sine function and n_{exci} is the number of oscillations of the excitation signal performed at each frequency step. In order to define accurate stepped sine signals significant preliminary work has been led to locate unknown resonances of investigated modes. Finite element simulations and clamped tests of the instrumented blades have provided good approximations of the resonances [7]. Exploration tests have been performed over a large frequency range to locate experimentally the resonances of the rotating fan. Other exploration tests have been performed to investigate stepped sine parameters influence over frequency response measurements. Stepped sine signal parameters have been defined according to determination rules:

- f_{ini} and f_{end} are defined in order to be able to perform analysis on the 3 dB frequency bandwidth of all investigated modes with nodal diameter
- δf is defined to have from five to ten measurement points inside the 3 dB frequency bandwidth of investigated modes to achieve fine description of resonance and precise estimation of modal damping ratios
- n_{exci} is taken high enough to measure quasi-stationary frequency response and avoid sweeping effects altering the frequency response measurements.

Moreover, the presented results use stepped sine with increasing frequencies $f_{ini} < f_{end}$. Frequency responses are obtained from discrete Fourier transform over a constant number of excitation oscillations at steady state for each frequency step. Frequency response functions are then computed by dividing the frequency response of a gauge in each blade by the discrete Fourier transform of the reference signal $u_{p=0}(t)$ over the same oscillations (see equation 1). Hence, the measured frequency response functions have size $n_s \times 1$. Figure 3 illustrates frequency response functions around two investigated modes for three blades. Repeatability tests have been performed to measure the stability of measurements against time and potential experimental conditions influence. Measurements with an identical set of experimental parameters has been considered repeatable when two frequency response functions have less than 10% difference of amplitude at resonance and resonance frequency shift less than $1.5 \cdot 10^{-3}$ UF. A normalized frequency unit UF is used in this article to preserve industrial confidentiality.

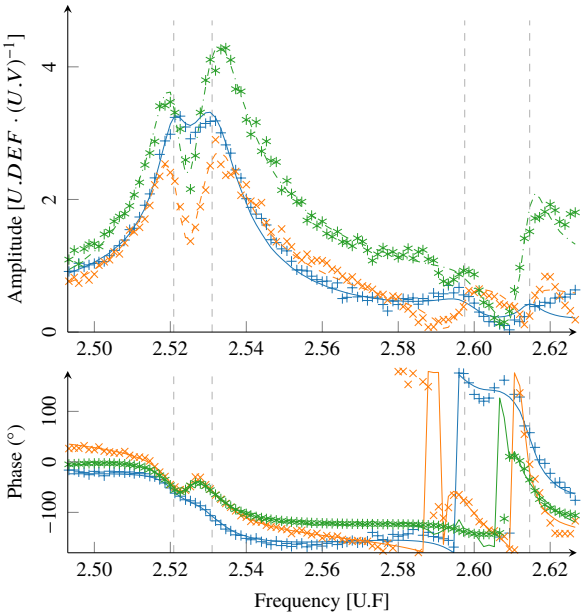

(a) *mode 2B at* $70\%\Omega_n$ *with* $d = 2$ *(*$n_m = 4$*)*

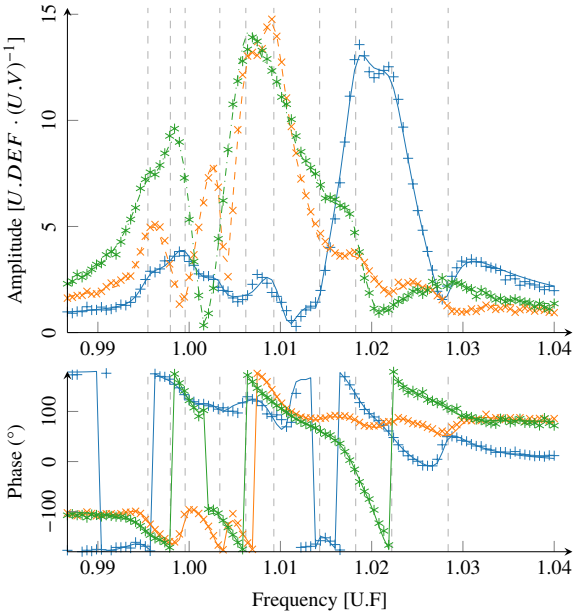

(b) *mode 1B at* $70\%\Omega_n$ *with* $d = 4$ *(*$n_m = 10$*)*

Figure 3: *Frequency response functions around two investigated modes at three sectors. Measurement points (+, ×, ∗) and fitting curves (— , - - , ···) are plotted for* $p = 1, 9, 18$*. Guidelines (- -) express identified natural frequencies.*

2 Modal parameters estimation

Modal parameters are estimated from frequency response function measurements, further abbreviated FRF. Figure 3 illustrates FRF measurements for three different blades around the two investigated blade modes at $70\%\Omega_n$. Among modal identification methods frequency domain techniques have been preferentially chosen as they are particularly adapted to estimate modal parameters from measured FRF data. The "Least Square Complex Frequency" technique [10] has been applied on these measurements without performing successful fitting. A more recently proposed estimation technique "Least Square Rational Function" has shown satisfying modal parameters estimation performance over the measured FRF data. Thus, this method has been applied to estimate poles of the system assuming knowledge of the order of the system. Residues of modal decomposition of estimated frequency response functions are computed from poles estimation results using a more classic least square approach. Then, model order determination is performed using heuristic techniques. Figure 4 illustrates the steps of the estimation process which are further discussed in the following subsections.

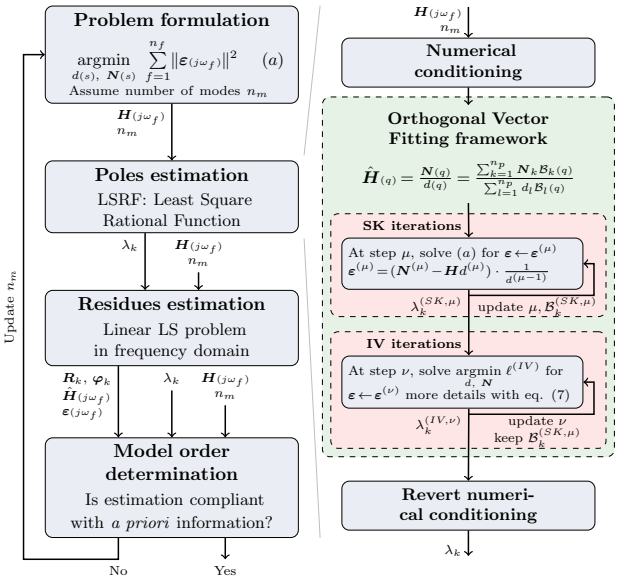

Figure 4: *Flowchart of the estimation process: overview of the complete process (left) and details of LSRF (right).*

2.1 Poles estimation

Poles estimation has been performed using "Least Square Rational Functions" (LSRF). This technique proposes to express the estimated frequency response function as a ratio of a multivariate numerator function divided by a common scalar denominator function such taking into account the multi-ouput nature of data measurements. The nonlinear optimization problem of minimizing the least square error between measured and estimated frequency response functions is solved using linearized minimization problem iterations. First, "Sanathan and Koerner iterations" are performed which, if convergence is achieved, converge to an approximate solution of the nonlinear problem. The applied technique proposes to improve the performance of estimation by using a basis of representation which takes into account *a priori* knowledge of the poles location and an orthogonalization process. This framework of optimization is denoted "Orthogonal Vector Fitting". In order to improve the estimation performance, "Instrumental Variable iterations" are further performed. These second series of iterations focus on finding local optimum of the nonlinear problem starting from previous iterations results. In the following paragraphs these key features of the method are further described. Full explanations of the Least Square Rational Function are available in reference articles [11].

Consider a frequency response function measurement $\boldsymbol{H}(j\omega)$ and the estimated frequency response function $\hat{\boldsymbol{H}}(j\omega)$ expressed according to a chosen model structure. The error signal $\boldsymbol{\varepsilon}$, defined as the difference between the measured and estimated responses, is assumed to be a Gaussian white noise process. Considering such assumptions, the maximum likelihood principle leads to the least square problem explicitly written in equation (2). As mentioned in the previous paragraph, the estimated frequency response function is expressed as a ratio of a multivariate numerator function $\boldsymbol{N}(s)$ and a scalar denominator function $d(s)$. These functions of Laplace variable s are the unknowns of the problem. The least square problem introduces n_f the number of frequency measurements.

$$\underset{d(s),\,\boldsymbol{N}(s)}{\operatorname{argmin}} \left\{ \ell = \sum_{f=1}^{n_f} \|\boldsymbol{\varepsilon}(j\omega_f)\|_F^2 \right\} \tag{2}$$

$$\text{With} \quad \boldsymbol{\varepsilon}(s) = \hat{\boldsymbol{H}}(s) - \boldsymbol{H}(s) \quad \text{and} \quad \hat{\boldsymbol{H}}(s) = \frac{\boldsymbol{N}(s)}{d(s)}$$

In order to solve the identification problem with improved numerical conditioning LSRF technique maps the problem from the left half-plane of Laplace domain to the unit disk with $q(s) = \frac{\alpha+s}{\alpha-s}$ and $\alpha > 0$. Choosing this domain mapping leads to poles location in a more confined domain which in turn improves numerical conditioning. Parameter α can be designed to optimize the distribution of the poles in the unit disk. The method also applies a scaling over measurement values to improve numerical conditioning. Further explanations concerning domain mapping and data scaling is presented in reference articles [11]. The main improvements of numerical conditioning is performed by expressing the identification problem in the "Orthogonal Vector Fitting" framework. This framework is presented here as being the "Vector Fitting" framework with an orthogonalization process. The "Vector Fitting" framework improves accuracy of the solution by injecting prior knowledge of poles location in the basis functions used for fitting. This injection of prior knowledge of poles location is performed through a barycentric representation of the numera-

tor and denominator of the estimated frequency response function. The corresponding barycentric representation is expressed in equation (3) in the mapped domain and using mapped poles of the system $\bar{\lambda}$. For further details concerning the "Vector Fitting" techniques see references articles [12].

$$\text{For} \quad r(q) = d(q),\ N_{ij}(q) \qquad (3)$$
$$r(q) = \sum_{l=1}^{n_p} r_l \frac{1}{q - \bar{\lambda}_l}$$

Where r_l denotes the coefficient associated with the element of the representation basis indexed by l ranging from 1 to number of poles n_p. Injecting representation of equation (3) in model structure makes the numerator $\boldsymbol{N}(q)$ and denominator $d(q)$ unknown rational functions with known poles ζ_l given by prior knowledge over the system dynamics. Using the zero-pole-gain representation of the numerator and denominator one can verify that the zeros of $d(q)$ are the poles of the estimated transfer function, as shown in equation (4).

$$\text{For} \quad r(q) = d(q),\ N_{ij}(q) \quad r(q) = \frac{\prod_{k=1}^{n_p}(q - z[r]_k)}{\prod_{l=1}^{n_p}(q - \zeta_l)} \qquad (4)$$
$$\frac{\boldsymbol{N}(q)}{d(q)} = \frac{\prod_{k=1}^{n_p}(q - z[\boldsymbol{N}]_k)}{\prod_{l=1}^{n_p}(q - z[d]_l)}$$

Where $z[r]_k$ denotes the zero of the function $r(q)$ indexed by k. A main drawback of this approach concerns estimation of systems with closely located poles as the problem becomes ill-conditioned having some basis element too close one to another. Hence, it is important to transform the barycentric basis through an orthogonalization process. The "Orthogonal Vector Fitting" framework used for modal identification makes the barycentric vector fitting basis (see eq. 3) orthogonal with respect to the standard inner product on $L^2(\mathbb{U})$ where $\mathbb{U} = \{s : |s| = 1\}$ written in equation (5).

$$\langle x, y \rangle = \frac{1}{2\pi} \int_{-\pi}^{\pi} x(e^{j\omega}) y^*(e^{j\omega}) d\omega \qquad x,\ y \in L^2(\mathbb{U}) \qquad (5)$$

The full construction of the orthonormal basis gathering the functions $\mathscr{B}_l(q)$ is proposed in reference article [13]. In this discussion only the two main steps of the construction process are mentioned. First, construct an intermediate orthogonal basis by performing an analytic Gram-Schmidt orthogonalization of the barycentric basis functions. Second, use specific linear combination of the obtained basis to gather complex conjugate poles obtaining real impulse response for each basis element. Model structure of estimated frequency response function is written in equation (6).

$$\hat{\boldsymbol{H}}(q) = \frac{\boldsymbol{N}(q)}{d(q)} = \frac{\sum_{k=1}^{n_p} \boldsymbol{N}_k \mathscr{B}_k(q)}{\sum_{l=1}^{n_p} d_l \mathscr{B}_l(q)} \qquad (6)$$
$$\text{With} \quad \langle \mathscr{B}_k, \mathscr{B}_l \rangle = \delta_{kl}$$

Similarly to the vector fitting framework the poles of the estimated transfer function $\hat{\boldsymbol{H}}(q)$ are the zeros of the rational function $d(q)$.

To solve the fundamental nonlinear least square problem (equation 2) LSRF method proposes to use Sanathan and Koerner iterations [14], further abbreviated SK iterations. This strategy has been proposed by Sanathan and Koerner to improve the deficiencies of techniques which solve the linear least square optimization problem associated with $\tilde{\varepsilon}(q) = \varepsilon(q) d(q)$ which approximates the problem of equation (2). This linearization approach is typically used in Least Square Complex Frequency. To solve further the fundamental nonlinear problem SK iterations propose to iterate over steps μ solving the least square problem associated with $\boldsymbol{\varepsilon}^{(\mu)} = \frac{\boldsymbol{\varepsilon} d^{(\mu)}}{d^{(\mu-1)}}$ where $d^{(\mu-1)}$ is known from previous iteration and can be interpreted as an updated weight. Thus, the error at every iteration step μ is associated to a linear least square optimization problem in $d_k^{(\mu)}$, $\boldsymbol{N}_k^{(\mu)}$. Provided that the algorithm converges, the solved error converges to the error in equation (2). SK iterations have been proposed for ratio of two polynomials, but this approach is still particularly adapted to solve nonlinear least square problem in the "Orthogonal Vector Fitting" framework. Indeed, the iterative process can also include update of the representation basis $\mathscr{B}_k^{(\mu)}$ using results of the poles location at the previous step as prior knowledge of poles location. The convergence of SK iterations is not ensured, particularly with noise corrupted data, nonlinear system dynamic or inappropriate model order. The association of SK iterations with "Orthogonal Vector Fitting" framework partially solves these latter numerical issues. However, asymptotic behavior studies of SK iterations explain that even if convergence is achieved the convergence is not necessarily a stationary point of the fundamental nonlinear optimization problem [15].

In order to compensate potential SK iterations deficiencies LSRF technique proposes to refine solution using "Instrumental Variable" iterations, further abbreviated IV iterations. These iterations aim at finding a stationary point of the fundamental nonlinear problem. IV iterations solve the minimum of the gradients of the matrix $\boldsymbol{M} = \boldsymbol{\varepsilon}\boldsymbol{\varepsilon}^H$ across $N_{l,ij}$ and d_l coefficients using the basis obtained after SK iterations and within least square framework, written in equation (7).

$$\underset{d(s),\, \boldsymbol{N}(s)}{\operatorname{argmin}} \left\{ \ell^{(IV)} = \sum_{f=1}^{n_f} \sum_{l=1}^{n_p} \left\| \frac{\partial \boldsymbol{M}}{\partial \boldsymbol{N}_l}(j\omega_f) \right\|_F^2 + \left\| \frac{\partial \boldsymbol{M}}{\partial d_l}(j\omega_f) \right\|_F^2 \right\} \qquad (7)$$
$$\frac{\partial \boldsymbol{M}}{\partial r_l} = 2\boldsymbol{\varepsilon} \frac{\partial \hat{\boldsymbol{H}}}{\partial r_l} \quad \text{with} \quad r_l = d_l, N_{l,ij}$$

Least square optimization problem of equation (7) exhibits similar nonlinearities as SK iterations. So an equivalent procedure is used to linearize the optimization problem, *i.e.* at step ν solve with modified term $\boldsymbol{\gamma}^{(\nu)} = \frac{\boldsymbol{\gamma} d^{(\nu)}}{d^{(\nu-1)}}$ with

$\boldsymbol{\gamma} = \partial_{\boldsymbol{N}_l} \boldsymbol{M}$ or $\boldsymbol{\gamma}^{(v)} = \frac{\boldsymbol{\gamma}(d^{(v)})^2}{(d^{(v-1)})^2}$ with $\boldsymbol{\gamma} = \partial_{d_l} \boldsymbol{M}$. Further investigations over such Instrumental Variable methods as well as examples of performance of SK, IV and Gauss-Newton iterations are proposed in references [16]. This article also proposes another choice of representation basis leading to an optimal condition number thanks to bi-orthonormal polynomials basis with respect to a data-dependent bi-linear form. However, LSRF technique has performed successful fits of measurement data, thus this improvement path has not been tested on presented data.

2.2 Residues estimation

Estimation of residues has been performed using least square technique and poles estimation results. Residues, denoted by $\boldsymbol{R}_l$, are defined from the modal decomposition of the frequency response function written in the following equation.

$$\boldsymbol{H}(j\omega) = \sum_{l=1}^{n_m} \frac{\boldsymbol{R}_l}{j\omega - \lambda_l} + \frac{\boldsymbol{R}_l^*}{j\omega - \lambda_l^*} \tag{8}$$

Residues have the same size as frequency response functions, for processed measurement data size is $n_s \times 1$. The number n_m denotes the number of modes of the system, for the studied system $n_p = 2n_m$. Solution obtained through the poles estimation process could provide estimation for the residues. However, previous studies concerning performance of SK iterations observed that more accurate results are in general obtained estimating the residues from the modal decomposition [12]. The chosen residues estimation process consists in using least square framework to solve the overdetermined linear equation given by modal decomposition and estimated poles. The singular values of the matrix of the least square formulation have been investigated over a representative sample of measurement data. Terms corresponding to poles with negative imaginary part in equation (8) have been associated to a significant degradation of the condition number of the least square problem. In consequence, these non-resonant terms have been removed from the least square formulation leading to solve the overdetermined matrix of equation (9). The condition number improvement provided by the truncated formulation has been associated with a considerable gain of error fitting, keeping the non-resonant terms on data measurements of second bending mode in table 1 would lead to $\|\boldsymbol{\varepsilon}'_{|n_m=4}\|_F > 0.3$ instead of $\|\boldsymbol{\varepsilon}'_{|n_m=4}\|_F = 0.123$ obtained with equation (9). This increase of error fitting could lead to potential inappropriate increase of the model order which in turn could affect poles estimation accuracy.

$$\begin{bmatrix} \boldsymbol{H}(j\omega_1) \\ \vdots \\ \boldsymbol{H}(j\omega_f) \end{bmatrix} \underset{LS}{=} \begin{bmatrix} \frac{1}{j\omega_1 - \lambda_1} & \cdots & \frac{1}{j\omega_1 - \lambda_{n_m}} & 1 \\ \vdots & \cdots & \vdots & \vdots \\ \frac{1}{j\omega_f - \lambda_1} & \cdots & \frac{1}{j\omega_f - \lambda_{n_m}} & 1 \end{bmatrix} \begin{bmatrix} \boldsymbol{R}_1 \\ \vdots \\ \boldsymbol{R}_{n_m} \\ \boldsymbol{R}_\infty \end{bmatrix} \tag{9}$$

$$\hat{\boldsymbol{H}}(j\omega) = \sum_{l=1}^{n_m} \frac{\boldsymbol{R}_l}{j\omega - \lambda_l} + \frac{\boldsymbol{R}_l^*}{j\omega - \lambda_l^*} + \boldsymbol{R}_\infty$$

$$\text{With} \quad \omega_l = |\lambda_l| \quad \text{and} \quad \xi_l \omega_l = -\text{Re}(\lambda_l)$$

Where $\omega_1 .. \omega_f$ in the least square equation (9) denote the measured pulsations. To further improve numerical conditioning of residues estimation a residual term $\boldsymbol{R}_\infty$ has been added to the fit model. This residual term models contribution of modes with natural frequency higher than the investigated frequency band. Other residual terms correcting lower frequency mode contributions or perturbations of the measurement signals have been tested without being associated with significative singular values for the pseudo inverse problem. Therefore, these residual corrections have not been taken into account for residues estimation process. As the investigated frequencies are confined in a narrowband the corrections introduced by other frequency-dependent residual terms are relatively small.

Residues estimation have been used to classify identified modes according to their mode shape and amplitude of modal participation. For the particular case of the measurement data, the residues have size $n_s \times 1$ so mode shapes and residues are proportional. Therefore, diameter analysis of identified modes has been performed on normalized residues with respect to 2-norm. The identified modes have also been analyzed with respect to the amplitude of modal participation defined as the 2-norm of the modal participation at resonance.

$$\boldsymbol{\varphi}_l = \frac{1}{\|\boldsymbol{R}_l\|_2} \boldsymbol{R}_l \quad \text{Estimated mode shapes} \tag{10}$$

$$\alpha_l = \frac{\|\boldsymbol{R}_l\|_2}{|j\omega_l - \lambda_l|} \quad \text{Amplitude of modal participation} \tag{11}$$

Where l indexes identified modes. Figures 5 and 6 show spatial Fourier transform of estimated mode shapes for tests investigating second and first bending mode respectively. On figure 5, the observed nodal diameter content leads to identify the first mode as forward travelling mode with 2 nodal diameters tagged "2D" and the second mode as a backward travelling mode with 2 nodal diameters tagged "-2D". Figure 6 illustrates a more challenging analysis and exhibits the effect of model order determination over identified modes analysis. This challenging analysis is associated with a higher modal density observed for the first bending mode with nodal diameter family. The diameter analysis of first bending mode will be further discussed in the next subsection focusing on model order determination.

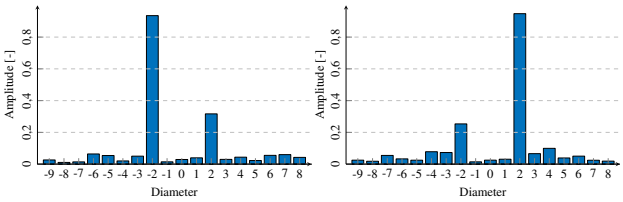

(a) *Second mode at* 2.521 $[U.F]$ **(b)** *First mode at* 2.531 $[U.F]$

Figure 5: *Amplitude of spatial discrete Fourier transform of identified mode shape ordered by amplitude of modal participation for 2B mode testing at* $70\%\Omega_n$ *and excitation pattern with* $d = 2$ *and for model order determination* $n_m = 4$.

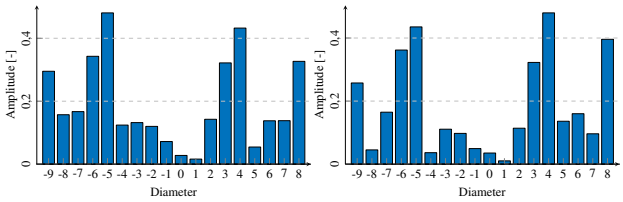

(a) *First mode with* $n_m = 8$ **(b)** *First mode with* $n_m = 10$

Figure 6: *Amplitude of spatial discrete Fourier transform of identified mode shape of the mode with maximal modal participation for 1B mode testing at* $70\%\Omega_n$ *and* $d = 4$ *with two different choices of model order.*

2.3 Model order determination

The previous subsections assumed model order has been determined. The model order is defined as the number of oscillating modes participating in the frequency response function. Determination of this order in the context of SK and IV iterations is an open problem. However, there exist some heuristic procedure to determine the model order mainly based on *a posteriori* analysis of estimation results. Model order determination process chosen for analyzing presented data is based on an analysis of the relative quadratic mean fitting error with respect to model order as well as a diameter analysis of the most excited modes.

The chosen model order determination scheme consists in defining a fitting error threshold observing relative quadratic mean square distance between repeatable measurements (see 1.2). Underneath the defined threshold estimated response is considered sufficiently accurate and increasing model order has been considered over fitting the data. Over fitted estimations identify spurious modes which can affect accuracy of other modal parameters estimation. Applying this model order determination rule is coherent with a hypothesis of time invariant system avoiding identification to go beyond repeatability limits of the measurement data. Using this framework, the distance between two repeatable measurements is interpreted as the effect of spurious modes which should not been taken into account in the identification process. The relative error fitting threshold has been estimated at $\varepsilon'_t = 0.17$ for parameters estimation concerning presented measurement data. This value has been taken as an approximation of the maximum relative quadratic mean square distance observed between two repeatable measurements for all investigated modes. This distance between repeatability measurements has been observed on measurements targeting second bending mode with $d = 2$, as shown in table 1. Figure 7 illustrates the evolution of the fitting error with the model order for the two investigated modes presented in figure 3 adding data of one repeatability test for each. The presented model order determination scheme would lead to choose $n_m = 4$ for the second bending mode and $n_m = 8$ for the first bending mode. This framework benefits from a simple test on error fitting to make model order determination.

However, first bending modes challenge the model determination scheme presented in the previous paragraph making classification of identified modes impossible with chosen model order. Concerning these data measurements, the criterion of "over-fitting" has been relaxed until classification of the identified modes using their mode shape and modal participation would match *a priori* information on the response of the system. This is illustrated by figure 6 showing estimation of mode shapes for the identified mode having the highest amplitude of modal participation for two choices of model order. Using the previous model determination scheme would lead to $n_m = 8$ exhibiting a diameter analysis with the highest nodal component at -5 (see fig. 6a) whereas the excitation pattern is set to $d = 4$. In such cases, the criterion of "over-fitting" has been relaxed to provide modal identification closer to *a priori* knowledge on the system response. Concerning figure 6, the criterion has been relaxed until $n_m = 10$ which leads to diameter analysis of the most excited mode having its highest nodal diameter component corresponding to $d = 4$ (see figure 6b). Still, the nodal components associated with -5 and 8 are high relatively to the component associated with 4 making the classification as a "4D" mode less clear-cut compare to second bending modes analysis.

Comparaison description	*Mode 2B*	*Mode 1B*
Distance between repeatable tests	0.170	0.133
Relative mean square fitting error ε'	0.123 ($n_m = 4$)	0.066 ($n_m = 10$)

Table 1: *Relative mean square distance between repeatable measurements compared with relative mean square fitting error for 2B mode with* $d = 2$ *and 1B mode with* $d = 4$ *at* $70\%\Omega_n$.

3 Results

The identification processes described in previous section has been applied to series of measurements to analyze sensitivity of extracted natural frequencies and damping ratios with respect to experimental parameters. First subsection discusses second bending mode results. Then, first bending mode results are discussed although uncertainties from

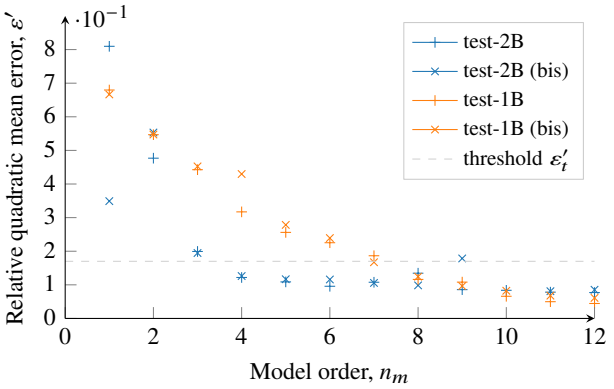

Figure 7: *Evolution of the relative quadratic mean square fitting error of FRF for two 2B mode tests with $d = 2$ and two 1B mode tests with $d = 4$ at $70\%\Omega_n$ with respect to the model order. Plotted data include the chosen fitting error threshold $\varepsilon'_t = 0.17$.*

identification processes are higher compare to second bending mode.

3.1 Second bending mode

Analysis of the second bending modes reveals sensitivity of extracted modal parameters with respect to rotation speed and amplitude of modal participation. Classification of identified modes thanks to their mode shapes (see 2.2) is used to add discussions over sensitivity with respect to excitation patterns.

Figure 8 focuses on the sensitivity of extracted natural frequencies and damping ratios of second bending mode with respect to rotation speed at constant level of excitation. Modal parameters are estimated with forward travelling wave excitations corresponding to $d = 2,3,4$ and maximum of amplitude of excitation a (see equation 1). Each test leads to modal parameters estimation of a mode having a major nodal diameter component at d and another at $-d$ using the presented identification procedure. Figure 8a shows natural frequencies increase with the rotation speed. This can be interpreted as spin stiffening effect. Analyzing the dependence of natural frequencies with respect to nodal diameter one makes the experimental observation that natural frequencies of the second bending mode increase with nodal diameter. A frequency split between forward and backward travelling modes with same nodal diameters can also be observed with a smaller natural frequency for the backward travelling mode. Dynamic of the system is subject to mistuning and Coriolis effects which could explain the observed frequency split. Note that natural frequencies are sensitive to amplitude of modal participation and these results are obtained with forward travelling wave excitations so forward travelling modes are typically more excited than backward travelling modes. This will be further discussed with figure 9a. Figure 8b shows extracted damping ratios globally decrease with rotation speed which is coherent with spin stiffening effect. Estimated damping

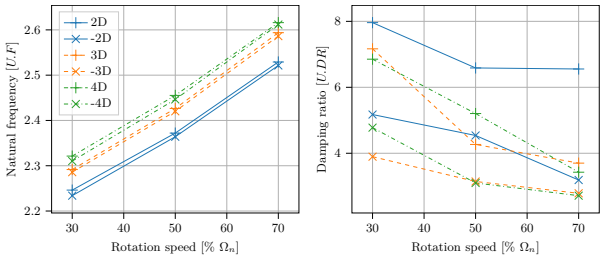

(a) *Natural frequency.* **(b)** *Damping ratio.*

Figure 8: *Sensitivity of modal parameters of 2B mode with respect to rotation speed at maximum excitation level and using forward travelling wave excitation patterns.*

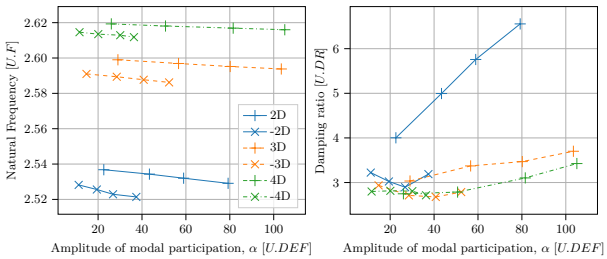

(a) *Natural frequency.* **(b)** *Damping ratio.*

Figure 9: *Sensitivity of modal parameters of 2B mode with respect to amplitude of modal participation α (equation 11) at $70\%\Omega_n$ using forward travelling wave excitation patterns.*

ratios results have more uncertainties than estimated natural frequencies making sensitivity analysis with respect to mode shape more difficult.

Figure 9 focuses on sensitivity of extracted natural frequencies and damping ratios for the second bending mode with respect to amplitude of modal participation for different excitation levels at $70\%\Omega_n$. Figure 9a shows natural frequencies and figure 9b damping ratios results. All extracted natural frequencies exhibit same sensitivity with respect to the amplitude of modal participation, decreasing when amplitude of modal participation increase. This frequency shift is compatible with friction in the system. Relative frequency shift observed for mode tagged "2D" from minimum excitation level to maximum is about $\Delta f_{2D}/f = -3 \cdot 10^{-3}$. As noted before the results are obtained with forward travelling excitation patterns hence forward travelling modes are more excited than backward travelling modes. This asymmetry of modal investigation can be observed on figure 9a, the forward travelling modes explore higher amplitude of modal participation compare to backward travelling modes. Observing the frequency split over comparable amplitude of modal excitation confirm frequency split effects discussed previously. Concerning mode tagged "2D" the relative frequency split at constant amplitude of modal participation is around $\Delta f_{\pm 2D}/f = 4 \cdot 10^{-3}$. Globally damping ratios increase or remain constant with increase of amplitude of modal participation (see figure 9b). Among extracted damping ratios mode "2D" takes

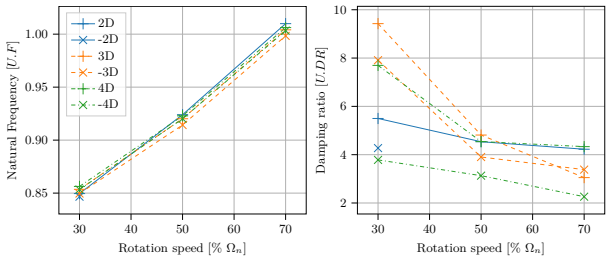

(a) *Natural frequency.* **(b)** *Damping ratio.*

Figure 10: *Sensitivity of modal parameters of 1B mode with respect to rotation speed at constant excitation level and using forward travelling wave excitation patterns.*

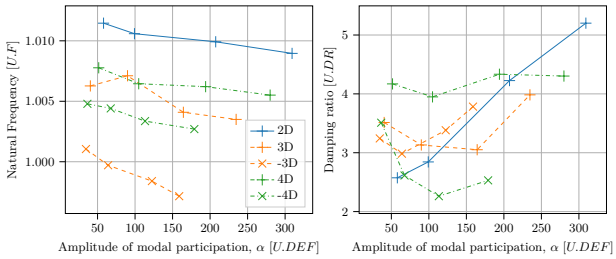

(a) *Natural frequency.* **(b)** *Damping ratio.*

Figure 11: *Sensitivity of modal parameters of 1B mode with respect to amplitude of modal participation* α *(equation 11) at* $70\%\Omega_n$ *using forward travelling wave excitation patterns.*

particularly high values and is more sensitive to amplitude of modal participation increase than "3D" and "4D".

3.2 First bending mode

Similar analysis have been performed concerning extracted parameters of first bending mode. Analysis provides less evidence of sensitivity, this is associated with more difficulties to estimate this family of modes.

The presented identification process did not succeed in extracted all modes of interest. The identification of first bending modes with mode shape close to a backward travelling pattern with two nodal diameters using forward travelling wave excitation has been too challenging for the presented identification process. Therefore, only few result points are available for extracted modes tagged "-2D". Figure 10 shows evolution of the extracted modal parameters of first bending mode with respect to rotation speed at constant amplitude of excitation, similarly to second bending mode analysis in figure 8. Extracted natural frequencies increase with rotation speed confirming spin stiffening observations. However, no particular evolution of natural frequencies with respect to nodal diameters can be established for first bending mode family. Damping ratios globally decrease with increase of the rotation speed which was also observed on second bending modes analysis. Comparing figure 10a with figure 8a provides illustration of higher modal density for mode 1B.

Analysis of first bending mode parameters with respect to amplitude of modal participation is illustrated in figure 11, similarly to second bending mode in figure 9. Extracted natural frequencies globally decrease when amplitude of modal participation increase which is a common feature of first and second bending modes observations. On figure 11a, the relative frequency shift for mode tagged "2D" from minimum excitation to maximum is about $\Delta f_{2D}/f = -2 \cdot 10^{-3}$ close to the value for the second bending mode. For mode tagged as "3D" and "4D" a frequency split is observed also with backward travelling modes having lower natural frequencies than forward travelling modes. Comparing over similar amplitude of modal participation the relative frequency split for mode tagged "3D" is approximately $\Delta f_{\pm 3D}/f = 5 \cdot 10^{-3}$. Note that the distance between natural frequencies of modes tagged "3D" and "4D" is approximately $\Delta f_{3D/4D}/f = 1 \cdot 10^{-3}$, which is smaller than the frequency split of mode "3D". Figure 11a brings additional evidence of higher modal density for first bending modes compare to second bending mode. To include damping in the discussion of modal density one can define a modal density indicator such as $\delta = \Delta f / \Delta_{3dB} f$ ratio of distance between natural frequencies and average 3 *dB* frequency bandwidth which includes damping ratio information. Comparing modes "3D/4D" of first bending mode with modes "3D/4D" of second bending mode one obtains $\delta_{1B} = 0.25$ compare to $\delta_{2B} = 2$. These indicator values show how much modal density of the first bending mode is higher than second bending mode. Figure 11b shows less evidence of sensitivity of damping ratios with respect to amplitude of modal participation. Still damping ratio of mode tagged "2D" exhibits significative increase with amplitude of modal participation whereas taking similar value compare to other nodal diameter modes. This is different from the second bending mode case where mode "2D" exhibits significantly higher values of damping ratio compare to other modes.

Conclusion

Experimental modal analysis of a full-scale rotating fan in vacuum conditions is presented from testing protocol to sensitivity analysis of modal parameters. Excitations are provided through piezoelectric actuators imposing a travelling wave with stepped frequency in order to investigate precise dynamics of the system. First blade bending mode challenges identification techniques, hence key features of the applied poles estimation technique have been reviewed, and special attention have been taken to have appropriate numerical conditioning for residues estimation. Heuristic remedies based on repeatability tests results and *a priori* knowledge over the system response have been proposed to determine model order. Observed modal parameters sensitivities are compatible with dynamics of a system subject to spin stiffening and friction phenomena.

To further investigate extracted modal parameters evo-

lution it would be interesting to provide series of results with estimation of the uncertainties of the whole identification process. As results exhibit slightly nonlinear effects it would also be interesting to pursue discussion evaluating impact of linear vibrations assumption of the used estimation method. More generally, it would be interesting to discuss the influence of the identification technique over modal parameters results in order to make more robust analysis.

Acknowledgment

The authors are grateful to "Agence National de la Recherche" (France) for supporting PHARE#1 test rig through PIA EQUIPEX PHARE project (ANR-10-EQPX-0043), to Carnot Institute I@L and Safran Aircraft Engines for providing additional financial support as well as for giving permission to publish this work. The authors also thank coworkers working on PHARE#1 test rig, among them particular thanks go to L. Sanchez and T. Vadcard for valuable discussions and contributions to PHARE#1 projects.

Nomenclature

FRF	Frequency Response Function
LSRF	Least Square Rational Functions
SK, IV	Sanathan and Koerner, Instrumental Variables
1B, 2B mode	First and second blade bending mode
Ω_n	Nominal rotation speed of the fan specimen
$U.F$, $U.DR$	Normalized unit of frequency and damping ratio
$U.DEF$	Normalized unit of deformation
$U.V$	Normalized unit of voltage: $U.V = 20\,V$
n_s, n_{exci}	Number of sectors and oscillations of excitation
n_p, n_m, n_f	Number of poles, modes and frequency points
$L^2(\mathbb{U})$	Quadratically integrable functions on unit circle
$\|.\|_2$, $\|.\|_F$	2-norm vector, Frobenius norm
s, q, ω	Laplace, mapped Laplace, pulsation variables
$\boldsymbol{H}(j\omega)$, $\hat{\boldsymbol{H}}(j\omega)$	FRF from measurement data, from estimation
$\boldsymbol{N}(j\omega)$, $d(j\omega)$	Numerator and denominator of estimated FRF
λ, $\bar{\lambda}$, ζ	Pole, mapped pole and pole *a prior* known
ε_t'	Relative quadratic mean error threshold
ω_l, ξ_l	Natural pulsation and damping ratio of mode l

References

[1] K. D'Souza et al. "A new experimental facility for characterizing bladed disk dynamics at design speed". In: *AIAA Journal* 58.6 (2020), pp. 2682–2690. DOI: 10.2514/1.j058682.

[2] E. Kurstak and K. D'Souza. "An experimental and computational investigation of a pulsed air-jet excitation system on a rotating bladed disk". In: *J. Eng. Gas Turbines Power* 143.1 (2021), p. 011017. DOI: 10.1115/1.0002901v.

[3] G. K. Lopp and J. L. Kauffman. "An experimental study of resonance frequency detuning applied to blade mistuning". In: *Turbo Expo: Power for Land, Sea, and Air*. American Society of Mechanical Engineers. 2018. DOI: 10.1115/gt2018-76834.

[4] D. Laxalde, C. Gibert, and F. Thouverez. "Experimental and numerical investigations of friction rings damping of blisks". In: *Turbo Expo: Power for Land, Sea, and Air*. 2008, pp. 469–479. DOI: 10.1115/gt2008-50862.

[5] C. Gibert. "Fitting measured frequency response using non-linear modes". In: *Mechanical systems and signal processing* 17.1 (2003), pp. 211–218. DOI: 10.1006/mssp.2002.1562.

[6] A. Mabilia et al. "Modal testing of a full-scale rotating woven composite fan using piezoelectric excitation". In: *International Conference on Rotor Dynamics*. Springer. 2018, pp. 291–305. DOI: 10.1007/978-3-319-99270-9_21.

[7] A. Mabilia et al. "Nonlinear forced response of a composite fan blade actuated by piezoelectric patches: Simulation and testing". In: *Nonlinear Dynamics, Volume 1*. Springer, 2019, pp. 351–362. DOI: 10.1007/978-3-319-74280-9_37.

[8] M. Friswell and J. Penny. "Stepped sine testing using recursive estimation". In: *Mechanical Systems and Signal Processing* 7.6 (1993), pp. 477–491. DOI: 10.1006/mssp.1993.1028.

[9] M. I. Friswell and J. E. T. Penny. "A Comparison of Two Recursive Estimators for Stepped Sine Testing". In: 11th International Modal Analysis Conference. 1993.

[10] P. Verboven. "Frequency-domain system identification for modal analysis". PhD thesis. 2002.

[11] A. A. Ozdemir and S. Gumussoy. "Transfer function estimation in system identification toolbox via vector fitting". In: *IFAC-PapersOnLine* 50.1 (2017), pp. 6232–6237. DOI: 10.1016/j.ifacol.2017.08.1026.

[12] B. Gustavsen and A. Semlyen. "Rational approximation of frequency domain responses by vector fitting". In: *IEEE Transactions on power delivery* 14.3 (1999), pp. 1052–1061. DOI: 10.1109/61.772353.

[13] B. Ninness and F. Gustafsson. "A unifying construction of orthonormal bases for system identification". In: *IEEE Transactions on automatic control* 42.4 (1997), pp. 515–521. DOI: 10.1109/9.566661.

[14] C. Sanathanan and J. Koerner. "Transfer function synthesis as a ratio of two complex polynomials". In: *IEEE transactions on automatic control* 8.1 (1963), pp. 56–58. DOI: 10.2172/4690788.

[15] A. H. Whitfield. "Asymptotic behaviour of transfer function synthesis methods". In: *International Journal of Control* 45.3 (1987), pp. 1083–1092. DOI: 10.1080/00207178708933791.

[16] R. Van Herpen, T. Oomen, and M. Steinbuch. "Optimally conditioned instrumental variable approach for frequency-domain system identification". In: *Automatica* 50.9 (2014), pp. 2281–2293. DOI: 10.1016/j.automatica.2014.07.002.